JOURNAL OF GEOPHYSICAL RESEARCH, VOL. 103, NO. B5, PAGES 9721–9738, MAY 10, 1998

Anomalous rotation of the inner core and the toroidal magnetic field

Jonathan Aurnou, Daniel Brito,[1] and Peter Olson

Department of Earth and Planetary Sciences, Johns Hopkins University
Baltimore, Maryland

Abstract. We use numerical calculations of magnetic induction by axisymmetric motions in a spherical shell of conducting fluid to investigate the relationship between the Earth's toroidal magnetic field and the time-dependent anomalous rotation of the solid inner core. We compute the induced toroidal magnetic field and inner core rotation maintained by the interaction of time-independent, axisymmetric outer core fluid flow with models of the poloidal magnetic field. Three possible models of the azimuthal flow in the outer core are investigated: two thermal wind flows inside the tangent cylinder (predicted by some numerical models of the geodynamo) and a columnar flow outside the inner core tangent cylinder inferred from the geomagnetic westward drift. Results indicate that electromagnetic torques tightly couple the inner core rotation to the fluid motion. Electromagnetic spin-up of the inner core occurs through damped torsional oscillations with periodicity near 4 years depending on the strength of the poloidal magnetic field. In steady state the thermal winds inside the tangent cylinder generate a peak toroidal field of 25 mT accompanying a prograde inner core rotation rate of 1°/yr. In contrast, the columnar westward drift model generates toroidal field with peak intensity near 4 mT and a small, retrograde anomalous inner core rotation of −0.013°/yr. The weak retrograde motion of the inner core produced by electromagnetic coupling to the westward drift cannot explain the seismically inferred prograde anomalous rotation.

1. Introduction

The first suggestion of anomalous inner core rotation was made by *Gubbins* [1981] who argued that the inner core is unlikely to rotate at precisely the same angular velocity as the mantle, owing to the low viscosity of the fluid outer core and electromagnetic torques associated with the geodynamo acting on the electrically conducting inner core. Gubbins demonstrated that electromagnetic torques couple the rotation rate of the inner core to the outer core fluid motion and, when perturbed, the inner core will spin-up into rotational equilibrium via damped torsional oscillations with periods near 6 years, the precise value depending on the intensity of the poloidal field near the inner core boundary (ICB). However, the full significance of Gubbins' work was not appreciated until *Glatzmaier and Roberts* [1995a, b] produced a three-dimensional convectively driven numerical model of the geodynamo which featured a persistent superrotation of the inner core of roughly 2°/yr. Several seismic studies have identified prograde superrotation of the inner core relative to the mantle. *Song and Richards* [1996] obtained a 1.1°/yr prograde (eastward) rotation of the inner core relative to the mantle, and *Su et al.* [1996] obtained a 3°/yr prograde rotation rate. *Creager* [1997] has also inferred a prograde anomalous rotation, although much slower, about 0.25°/yr.

In addition to observational questions such as the precise magnitude of the present-day anomalous inner core rotation rate and whether it represents a persistent or a transient effect, there are also geodynamical questions concerning the origin of the inner core superrotation and its connection with the dynamo mechanism. Specifically, the superrotation rates inferred by *Song and Richards* [1996] and *Su et al.* [1996] imply much larger angular velocities of the outer core fluid than were previously thought, which has important implications for the process of toroidal field generation.

Prior to the detection of anomalous inner core rotation, the main evidence for azimuthal flow in the outer core fluid came from the westward drift of the geomagnetic field. Westward drift deduced from the pattern of geomagnetic secular variation indicates retrograde motion of the fluid below the core-mantle boundary (CMB) at an average rate of approximately −0.2°/yr [*Bloxham*

[1]Now at Laboratoire de Géophysique Interne et Tectonophysique, Observatoire de Grenoble, Grenoble, France.

Paper number 97JB03618.
0148-0227/98/97JB-03618$09.00

et al., 1989]. The correlation between changes in westward drift and the decade-scale fluctuations in the rotation rate of the mantle implies that the momentum of the fluid involved in the westward drift is quite large and has led to the idea that the pattern of westward drift results from differential rotation of coaxial cylinders of fluid [*Jault et al.,* 1988], as illustrated in Figure 1c. It has long been recognized that the shear between differentially rotating fluid cylinders is an efficient mechanism for toroidal field generation through the so-called ω effect [*Elsasser*, 1946], and in many geodynamo models this is the primary source of toroidal field [*Hollerbach*, 1996].

However, recent numerical modeling of the structure of convection in the outer core [*Olson and Glatzmaier*, 1995; *Glatzmaier and Roberts*, 1995a, b] has identified another source of toroidal field, high-velocity thermal wind shear flows located inside the inner core tangent cylinder, as illustrated in Figures 1a and 1b. Thermal winds are equally effective at generating toroidal field as the flow associated with westward drift and furthermore, they offer an explanation for prograde inner core rotation [*Aurnou et al.,* 1996; *Glatzmaier and Roberts*, 1996]. Electromagnetic torques act to couple the motion of the inner core to the prograde motion of the surrounding fluid, and the inner core rotates with the fluid adjacent to the inner core boundary, but at a slightly reduced rate.

In addition to electromagnetic coupling, two other mechanisms have been proposed to explain the anomalous rotation: tidal spin-down of the mantle relative to the inner core [*Su et al.,* 1996] and long-period inner core oscillation in response to torques exerted by the gravitational field of the mantle [*Buffett*, 1996]. Both of these alternative mechanisms are likely to affect inner core rotation to some degree. However, the electromagnetic coupling mechanism predicted by *Gubbins'* [1981] original analysis (and substantiated by the recent dynamo calculations of *Glatzmaier and Roberts* [1996] and *Kuang and Bloxham* [1997]) provides amply strong torques to drive the anomalous rotation of the inner core.

In this paper we use numerical models of toroidal magnetic field generation by an imposed axisymmetric core flow to compute the anomalous inner core rotation resulting from electromagnetic torques. In our previous paper [*Aurnou et al.,* 1996] we presented a simplified analytical model of inner core superrotation based on electromagnetic coupling between the inner core and a "thermal wind" shear flow located inside the tangent cylinder of the inner core that reproduces the essential physics found in the *Glatzmaier and Roberts* [1995a, b, 1996] dynamo calculations. Here we extend that model to an axisymmetric spherical geometry with time dependence, and we investigate the anomalous inner core rotation produced by a second thermal wind model and an azimuthal flow inferred from the geomagnetic westward drift.

2. Description of the Models

The Earth's core is modeled with a solid inner core and a liquid outer core, both having a uniform electrical conductivity. The solid mantle is treated as electrically insulating, and its rotation rate is assumed to be constant. A steady axisymmetric dipolar magnetic field is imposed throughout the core, and a steady azimuthal flow is imposed in the liquid outer core. Figure 1 illustrates the three core flow models that are used to calculate the toroidal magnetic field and the anomalous inner core rotation. We do not consider the action of the so-called "magnetic wind" acting back on the motion of

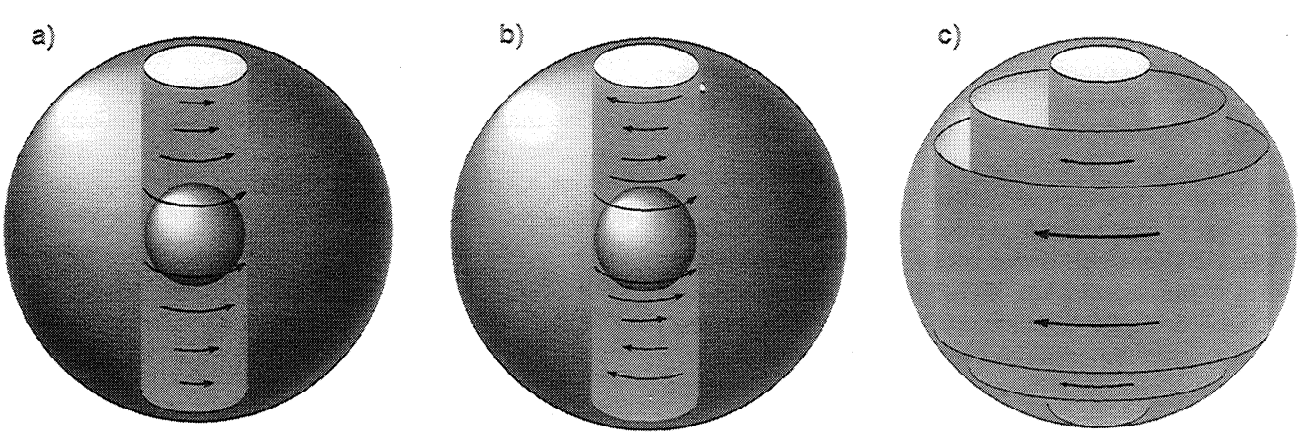

Figure 1. Sketches of the three models of azimuthal fluid flow in the outer core. (a) Prograde thermal wind inside the inner core tangent cylinder (model 1). (b) A second thermal wind flow model, called the X wind (model 2), has strong prograde flow inside the tangent cylinder surrounding the inner core and an equally strong retrograde flow at the core-mantle boundary (CMB). (c) The flow in model 3 consists of retrograde differential fluid motion on concentric cylinders outside the tangent cylinder.

the outer core fluid, although the magnetic wind represents an additional source of azimuthal motion in the fluid (R. Hollerbach, personal communication, 1997).

The rotation rate of the inner core is allowed to vary through the action of applied torques. We use free slip boundary conditions at the inner core boundary, and we ignore the effects of topography on the ICB, so the inner core rotation rate is affected only by electromagnetic torques. The outer core flow interacts with an imposed poloidal magnetic field, inducing toroidal field which diffuses throughout the core and produces electromagnetic torques on the inner core.

Flow model 1, illustrated in Figure 1a, consists of a thermal wind shear flow located inside the tangent cylinder similar to the flow used in our analytical model. Flow model 2, shown in Figure 1b, consists of a thermal wind flow model with the pattern of shear kinematically similar to the thermal wind found in the dynamo calculations of *Glatzmaier and Roberts* [1996]. Flow model 3, shown in Figure 1c, consists of differential rotation of concentric cylinders of fluid in the region outside the tangent cylinder. The distribution of differential rotation is obtained from the pattern of zonal fluid velocities derived from secular variation of the geomagnetic field [*Jault et al.*, 1988], and this motion is kinematically similar to the *Kuang and Bloxham* [1997] dynamo.

3. Governing Equations

The induction equation for the magnetic field is

$$\frac{\partial \mathbf{B}}{\partial t} = \nabla \wedge (\mathbf{u} \wedge \mathbf{B}) + \eta \nabla^2 \mathbf{B} \tag{1}$$

where $\mathbf{B} = (B_r, B_\theta, B_\phi)$ is the magnetic induction in spherical (r, θ, ϕ) coordinates, $\mathbf{u}$ is the fluid velocity, η is the magnetic diffusivity, and t is time.

Anomalous rotation of the inner core about the polar $\hat{z}$ direction is governed by the following angular momentum balance:

$$I \frac{d(\Delta\Omega_{IC})}{dt} = \Gamma \tag{2}$$

where I is the polar moment of inertia of the inner core, $\Delta\Omega_{IC}$ is the anomalous angular velocity of the inner core, and Γ is the $\hat{z}$ component of torque acting on the inner core. In our model, we consider only the electromagnetic torque on the inner core. This torque can be written as a surface integral over the ICB [*Rochester*, 1962]:

$$\Gamma = \frac{1}{\mu} \int_{\mathrm{ICB}} B_r B_\phi \, r \sin\theta \, dS \tag{3}$$

where μ is the magnetic permeability (see Table 1).

The axisymmetric magnetic field is decomposed into poloidal and toroidal parts (labeled P and T, respectively):

$$\mathbf{B} = \mathbf{B}_P + \mathbf{B}_T \tag{4}$$

Both parts can be expressed in terms of scalar variables, A_ϕ and B_T [*Moffatt*, 1978]. The poloidal part is

$$\mathbf{B}_P = \nabla \wedge \hat{\phi} A_\phi \tag{5}$$

with components

$$(B_r, B_\theta) = \left(\frac{1}{r \sin\theta} \frac{\partial}{\partial \theta} (\sin\theta A_\phi), -\frac{1}{r} \frac{\partial}{\partial r} (r A_\phi) \right) \tag{6}$$

and the toroidal part is

$$\mathbf{B}_T = \hat{\phi} B_T \tag{7}$$

Substituting (5), (6) and (7) into (1), the induction equation for the toroidal field subject to an axisymmetric, azimuthal flow $\mathbf{u} = \hat{\phi} u_\phi$ is

$$\left(\frac{\partial}{\partial t} - \eta (\nabla^2 - \frac{1}{s^2}) \right) B_T = B_r \frac{\partial u_\phi}{\partial r} + \frac{B_\theta}{r} \frac{\partial u_\phi}{\partial \theta} \tag{8}$$

where $s = r\sin\theta$ is the cylindrical radial coordinate.

The boundary condition for axisymmetry requires

$$B_T = 0 \quad \text{at} \quad \theta = 0, \pi \tag{9}$$

which forces the toroidal field to vanish along the rotation axis. Assuming the mantle to be an electrical insulator requires the condition

$$B_T = 0 \quad \text{at} \quad r = R_C \tag{10}$$

where R_C is the radius of the core (see Table 1).

Table 1. Parameter Values Used in Numerical Simulations of Anomalous Inner Core Rotation

Symbol	Parameter	Value
$\Delta\Omega_{TW}$	maximum rate of thermal wind	1°-3°/yr
$\Delta\Omega_{XW}$	maximum rate of X wind	1°-3°/yr
R_C	core radius	3.48×10^6 m
R_I	inner core radius	1.22×10^6 m
I	inner core moment of inertia	5.87×10^{34} kg m^2
μ	magnetic permeability	$4\pi \times 10^{-7}$ H/m
η	core magnetic diffusivity	2.65 m^2/s
B_o	typical magnetic field on CMB	0.37 mT

CMB, core-mantle boundary.

At the ICB the tangential electric field must be continuous, leading to the following condition:

$$\frac{\partial B_T}{\partial r}\Big|_{\mathrm{ICB-}}^{\mathrm{ICB+}} = -\frac{\Delta v B_{p_\perp}}{\eta} \tag{11}$$

where Δv is the jump in velocity across the ICB and $B_{p_\perp}$ is the magnitude of the poloidal magnetic field that is perpendicular to the boundary. In our calculations, we directly integrate the induction equation across the ICB. This technique approximates the velocity discontinuity resulting from a free slip boundary condition with a sharp velocity gradient at the ICB, $\Delta v/\Delta r$, where Δr is the radial numerical grid spacing. This representation introduces an error into our solutions that is of the order $\Delta r/R_C$, which is less than 1% in all the calculations presented.

4. Poloidal Magnetic Field Models

Two imposed poloidal magnetic field models are used inside the core: a fundamental mode, current-carrying dipole field and a uniform $\hat{z}$-directed magnetic field. These two poloidal fields have the same potential field solution at the CMB but strongly differ inside the core. The current-carrying dipole is the slowest freely decaying field inside the core. The uniform $\hat{z}$ magnetic field results from an externally imposed dipole field diffusing into the core. The uniform field, though somewhat less physically plausible, is identical to the magnetic field used in our analytical model [*Aurnou et al.*, 1996] and allows us to compare numerical and analytical results.

4.1. Current-Carrying Dipole Magnetic Field

The current-carrying dipole field is generated from a poloidal potential A_ϕ in (5) of the form

$$A_\phi = (\pi R_C) B_o \, J_1\left(\frac{\pi r}{R_C}\right) \sin\theta \tag{12}$$

This corresponds to the first fundamental mode of a freely decaying axial dipole field with a radial dependence given by the Bessel function [*Abramowitz and Stegun*, 1964]:

$$J_1(x) = \frac{\sin(x)}{x^2} - \frac{\cos(x)}{x} \tag{13}$$

This magnetic vector potential produces a magnetic field with intensity B_o on the north pole of the CMB.

4.2. Uniform Poloidal Field

The azimuthal component of the magnetic vector potential for a uniform field is

$$A_\phi = \frac{B_o}{2} r\sin\theta = \frac{B_o}{2} s \tag{14}$$

which produces a uniform magnetic field vector $B_o \hat{z}$ throughout the core.

5. Fluid Flow Models

The imposed axisymmetric flow fields consist of azimuthal fluid flows

$$u_\phi = s\omega \tag{15}$$

where the angular velocity ω can vary as a function of distance from the equatorial plane z and radius s in cylindrical coordinates. The inner core motion consists of solid body rotation. Consequently, inside the inner core $r \leq R_I$ we set

$$\omega = \Delta\Omega_{IC} \tag{16}$$

where $\Delta\Omega_{IC}$ is determined from (2) and R_I is the inner core radius (see Table 1).

5.1. Thermal Wind Flow (Model 1)

Our first model of a thermal wind located inside the inner core tangent cylinder is as follows (see Figure 1a). Within the tangent cylinder, in the region $s \leq R_I$ and $|z| \geq R_I$, we represent the angular velocity as a function of the z coordinate in (15) and set

$$\omega(z) = \Delta\Omega_{TW} \, z^* \tag{17}$$

where $z^* = (R_C - |r\cos\theta|)/(R_C - R_I)$ is the dimensionless depth below the CMB measured parallel to the rotation axis and $\Delta\Omega_{TW}$ is the maximum angular velocity of the fluid in the tangent cylinder relative to the mantle. This motion (equation (17)) consists of solid body rotation of the fluid in planes perpendicular to the rotation axis, with angular velocity decreasing with distance from the ICB.

By prescribing flow only within the tangent cylinder, a discontinuity in angular velocity at the tangent cylinder wall is produced. In reality, the change in angular velocity occurs continuously in a narrow, free shear layer, a so-called Stewartson layer at the tangent cylinder boundary [*Greenspan*, 1968; *Kleeorin et al.*, 1997; *Dormy et al.*, 1998]. We model the Stewartson layer by multiplying ω by a taper function Ψ_{St} defined by

$$\Psi_{St} = \frac{1}{2}\left[1 - \tanh\left(\frac{3(s - S_o)}{S_o - R_I}\right)\right] \tag{18}$$

where $s = r\sin\theta$ is the cylindrical radius, R_I is the inner core radius, and S_o is the location of the tangent cylinder. In the calculations presented here we have defined $S_o = 1270$ km in (18), which produces a 100 km thick Stewartson layer centered 50 km outside the radius of the inner core.

Another region where the thermal wind velocity is problematic is the corner region of the tangent cylinder, $|z| < R_I$, $s < R_I$, and $r > R_I$, which tapers down to a wedge at the equator. To avoid a shear singularity in the wedge, we hold the angular velocity constant at $\Delta\Omega_{TW}$ inside this region.

5.2. X Wind Flow (Model 2)

A second model of a tangent cylinder thermal wind we consider is an "X wind" flow model, so called because the velocity vectors trace out an "X" in each hemisphere (see Figure 1b). Model 2 is kinematically similar to model 1 except that the angular velocity is now

$$\omega = \Delta\Omega_{XW}\, z^* \tag{19}$$

where $\Delta\Omega_{XW}$ is the magnitude of the azimuthal velocity at $z = R_I$ and z^* is now

$$z^* = \frac{(R_C + R_I) - 2|r\cos\theta|}{R_C - R_I} \tag{20}$$

This model has zero angular velocity midway between R_C and R_I, whereas flow model 1 locates this zero at the CMB. Flow model 2 is very similar to the azimuthal flow field induced by the polar upwellings in the dynamo model of *Glatzmaier and Roberts* [1996].

5.3. Flow Derived From Geomagnetic Westward Drift (Model 3)

Prior to the inference of inner core superrotation, the westward drift of the surface magnetic field provided the basic velocity scale for core motions. Thus for comparison we include the case of the toroidal field generated by the zonal fluid velocities inferred from geomagnetic secular variation. In this westward drift model the flow is assumed to be on cylinders aligned with the rotation axis [*Jault et al.*, 1988]. Instead of the shear inside the tangent cylinder, where $\omega = \omega(z)$, the shear in the westward drift model is a function of cylindrical radius alone, $\omega = \omega(s)$, as shown in Figure 1c.

This westward drift model uses the data of *Jault et al.* [1988]. The azimuthal velocities from all epochs have been stacked into one data set and have been zonally averaged. The result of this averaging is seen in Figure 10a which shows the angular velocity as a function of colatitude. The profile by *Jault et al.* [1988] extends from 65°N to 65°S latitude and produces zero fluid flow inside the tangent cylinder. More recent inversions of the secular variation [*Jackson*, 1998] yield more complete azimuthal flows, which are nevertheless similar to Figure 10a.

The different numerical models are summarized in Table 2. Note that there is no westward drift model with a uniform $\hat{z}$ magnetic field. This is because the cylindrical fluid shear in the westward drift flow model will not induce any toroidal magnetic field.

Table 2. Numerical Models of Time-Independent, Axisymmetric Outer Core Fluid Flow and Poloidal Magnetic Field

Model	Fluid Flow Model	Poloidal Field Model
1a	thermal wind	current-carrying dipole
1b	thermal wind	uniform $\hat{z}$ field
2a	X wind	current-carrying dipole
2b	X wind	uniform $\hat{z}$ field
3	westward drift	current-carrying dipole

6. Numerical Techniques

Second-order central finite differences and explicit, first-order time stepping are used to solve (2), (3), (8), (9), and (10) in their nondimensionalized forms. Parameter values used in these equations are given in Table 1. The computational scheme calculates the electromagnetic torques on the inner core using (3) with the magnetic field values of the previous time step. The angular momentum balance (2) is updated with the new torque value. The time step is completed by solving the toroidal induction equation (8) with the new value of inner core angular velocity and subject to the application of the toroidal field boundary conditions (9) and (10).

A numerical grid in r and θ of 120 × 120 has been used in calculations that reach steady state in roughly 20,000 simulated years. This produces equidistant grid points with spacings of $\Delta r = 25$ km and $\Delta\theta = 1.5°$ and a simulated time step of roughly 1 month. Since we do not solve the equations in the innermost 500 km of the core, a total of 120 grid points with a 25 km step size comprise our radial grid. Numerical experiments were also run using grids of the order of 40 × 40. The 40 × 40 grids gave qualitatively similar results to the 120 × 120 grids, but the larger grid was found to be needed to effectively resolve the Stewartson layer.

Modeling of the spin-up process of the inner core has also been carried out by taking very small time steps, O(1 day), and running the code for at most 30 simulated years. These simulations are initialized with either imposed poloidal magnetic field configuration, flow model 1, and no motion of the inner core. In these spin-up calculations a 395 × 120 numerical grid is used for the current-carrying dipole field model. For the uniform field calculations a smaller computational shell grid is used. The shell is centered around the ICB and has a width of $0.1R_C$, which allows the use of a 50 × 50 grid. Both of these grids have an equidistant nodal spacing of $\Delta r = 7$ km radially. This grid spacing produces a simulated time step of 25 hours. Gradients in the θ direction were small, and fewer points were needed to achieve adequate θ resolution.

6.1. Thermal Wind Flow Results

The velocity field u_ϕ acts on the imposed poloidal magnetic field to induce toroidal fields, which in turn produce electromagnetic torques on the inner core. The exterior magnetic field at the CMB is constructed by using the present-day Gauss coefficient for the axial dipole field, $g_1^0 \simeq -30{,}000$ nT, from the International Geomagnetic Reference Field model [*IAGA Division V, Work-*

ing Group 8, 1996] and downward continuing to the CMB, assuming the mantle to be a perfect insulator. This yields a value of $B_o = -0.37$ mT in (12) and (14).

Figure 2 shows the results of a calculation after 25,000 simulated years for an imposed thermal wind of $\Delta\Omega_{TW} = 3°/\text{yr}$ interacting with a fundamental mode current-carrying dipole field (model 1a). The right side shows the angular velocity in shaded contours as well as lines of force of the poloidal field. The left side shows the shaded contours of the induced toroidal magnetic field intensity. The angular velocity increases linearly toward the ICB from zero at the CMB. The fluid rotates on solid-body discs at every level in z^*. The Stewartson layer truncation bends the angular velocity contours downward for $s > R_I$ so that large cylindrical fluid shears exist at the tangent cylinder wall and no further fluid motions exist outside of this shear layer. The contouring of the inner core is darker than that of the surrounding fluid in the "corner region" because the core is lagging behind the fluid.

The induced toroidal field contoured on the left side of Figure 2 is generated dominantly inside the tangent cylinder. The maximum toroidal field strength is located slightly below midheight and close to the boundary of the tangent cylinder. The effect of the Stewartson layer is clearly visible in the contours of the toroidal field.

Time series of the rotation rate of the inner core, the maximum toroidal field in the core, and the Joule heating in the core are plotted in Figure 3 for a 3°/yr thermal wind. The current-carrying dipole model reaches equilibrium with the inner core in prograde rotation, lagging the surrounding fluid by 29%, that is,

$$\Delta\Omega_{IC} = 0.71\,\Delta\Omega_{TW} \tag{21}$$

In this calculation the maximum imposed thermal wind velocity $\Delta\Omega_{TW}$ is 3°/yr and the seismically observable inner core rotation rate $\Delta\Omega_{IC}$ is 2.13°/yr (Figure 3a). As shown in Figure 3b, the maximum toroidal magnetic field generated by a 3°/yr thermal wind is on the order of 60 mT. The Joule heating in the core is about 600 GW for this flow (Figure 3c).

The calculation shown in Figure 4 is similar to Figure 2 except that a uniform poloidal magnetic field has been imposed on the thermal wind flow (model 1b). In this case the inner core again lags behind the surrounding fluid but by a smaller percentage than for the current-carrying dipole model. The toroidal field is centered closer to the CMB and the rotation axis than in the case shown in Figure 2. No evidence of a tangent cylinder is discernible in the toroidal field contours in Figure 4.

As shown in Figure 3a and Table 3, the inner core rotates at $\Delta\Omega_{IC} = 2.56°/\text{yr}$, which corresponds to inner core prograde rotation with a lag of 15% behind the imposed 3°/yr thermal wind velocity:

$$\Delta\Omega_{IC} = 0.85\,\Delta\Omega_{TW} \tag{22}$$

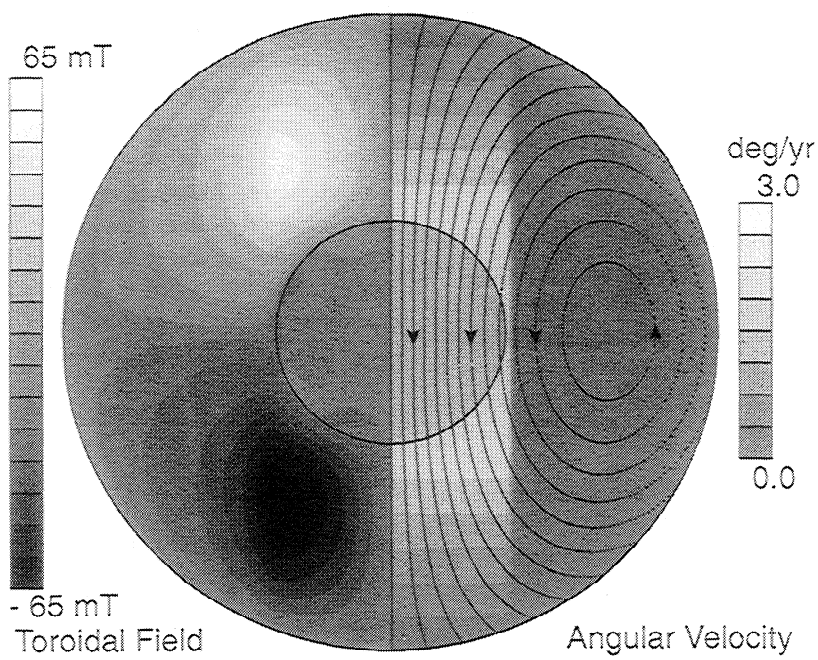

Figure 2. Steady state results of the model with a current-carrying dipolar magnetic field and the 3°/yr thermal wind flow (model 1a). Contours of angular velocity relative to the mantle of the outer core fluid flow and the solid inner core are shown on the right side. Dipole field lines are superimposed on the angular velocity contours. Shaded contours of the induced toroidal field in milliteslas are shown on the left side. The anomalous inner core rotation ($\Delta\Omega_{IC} = 2.13°/\text{yr}$) is indicated by the darker shading of the angular velocity contours inside the inner core relative to the surrounding fluid ($\Delta\Omega_{TW} = 3°/\text{yr}$). The maximum toroidal field is 62 mT.

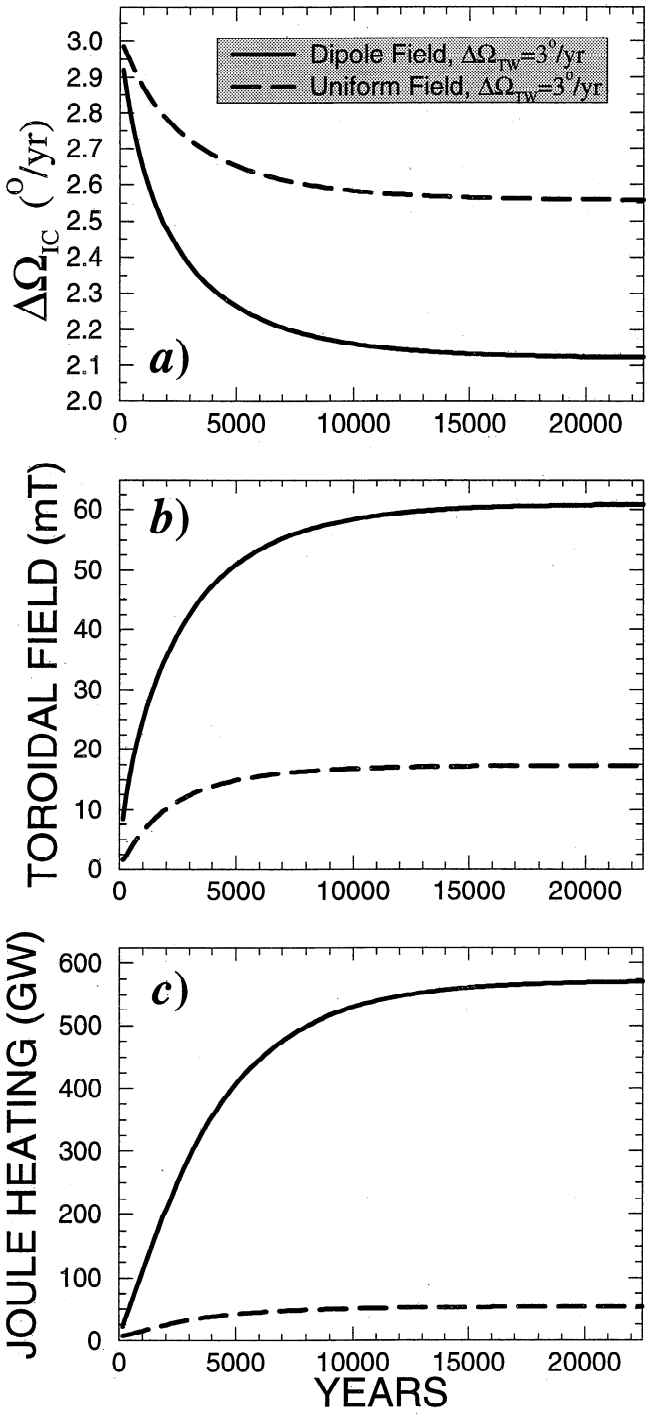

Figure 3. Time series plots of (a) the anomalous rotation of the inner core $\Delta\Omega_{IC}$, (b) the maximum induced toroidal magnetic field $B_{T\max}$, and (c) the Joule heating in the core resulting from a 3°/yr thermal wind acting on a current-carrying dipole and a uniform $\hat{z}$ poloidal magnetic field (model 1a shown in Figure 2 and model 1b in Figure 4). The calculations were made using a 120 × 120 grid for 25,000 simulated years. Steady state is reached after approximately 20,000 years.

The toroidal field equilibrates after 20,000 years and has a maximum value of roughly 20 mT, as shown in Figure 3b. This is a reduction by a factor of almost 3 from the toroidal fields found in the current-carrying dipole numerical solution and a factor of 2 from the analytical model [*Aurnou et al.*, 1996]. The Joule heating in the core is correspondingly decreased and is roughly 50 GW, as shown in Figure 3b.

Figure 5 shows the results of thermal wind model 1 simulations with $\Delta\Omega_{TW} = 1°/\text{yr}$. The inner core is again found to superrotate and lags behind the surrounding fluid by 15% in the uniform field model and by 29% in the current-carrying dipole field model. Relationships (21) and (22) are found to be valid for all values of the maximum thermal wind velocity.

6.2. X Wind Flow Results

Figure 6 shows the results of a calculation after 25,000 simulated years for an imposed X wind flow of $\Delta\Omega_{XW} = 3°/\text{yr}$ interacting with a fundamental mode current-carrying dipole field (model 2a). The shaded contours on the right side show how the angular velocity increases linearly from $-3°/\text{yr}$ at the CMB to $+3°/\text{yr}$ at $z = R_I$. The Stewartson layer truncation bends the angular velocity contours downward for $s > R_I$ and $z < (R_C + R_I)/2$ but bends the angular velocity contours upward for $s > R_I$ and $z > (R_C + R_I)/2$. This changes the net effect of the Stewartson layer truncation between model 2 and model 1.

In this case, the inner core equilibrates with a prograde rotation rate of 1.87°/yr, which corresponds to an inner core lag of 37% behind the surrounding fluid

$$\Delta\Omega_{IC} = 0.63\ \Delta\Omega_{XW} \tag{23}$$

The maximum toroidal field induced in this model is almost 80 mT (see the shaded contours on the left side of Figure 6), and the Joule dissipation is nearly 900 GW. The toroidal field maximum is located inside the tangent cylinder just below midheight. The Stewartson layer is visible in the shaded contours of the toroidal field on the left side of Figure 6, although it has less effect on the toroidal field than in the case shown in Figure 2.

Figure 7 shows the results of a calculation after 25,000 simulated years for an imposed X wind flow of $\Delta\Omega_{XW} = 3°/\text{yr}$ interacting with the uniform $\hat{z}$ magnetic field (model 2b). The inner core anomalous rotation is 2.12°/yr prograde, which corresponds to an inner core lag of 29% behind the surrounding fluid, so that

$$\Delta\Omega_{IC} = 0.71\ \Delta\Omega_{XW} \tag{24}$$

The maximum toroidal magnetic field induced in this model is about 35 mT and is located close to midheight inside the tangent cylinder and closer to the rotation axis than the toroidal field of model 2a. Thus the location of the toroidal field maxima are similar in models 1 and 2. The Joule dissipation is just under 200 GW in this case.

The results in Figures 3 and 5 and Table 3 indicate that the maximum induced toroidal field is a linear func-

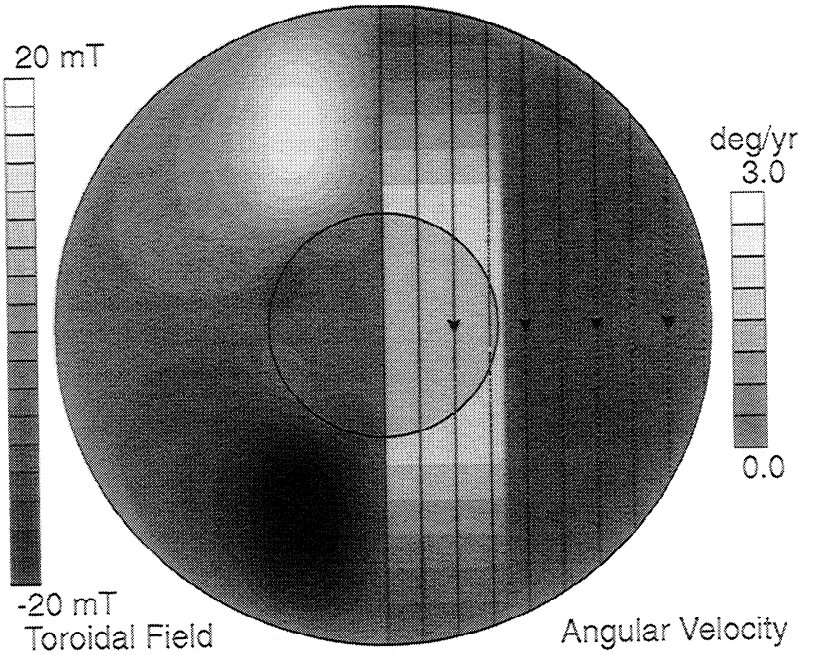

Figure 4. Steady state results of the model with a uniform $\hat{z}$ poloidal magnetic field and the 3°/yr thermal wind flow (model 1b). Contours of angular velocity relative to the mantle of the outer core fluid flow and the solid inner core are shown on the right side. Uniform $\hat{z}$ field lines are superimposed on the angular velocity contours. Shaded contours of the induced toroidal field in milliteslas are shown on the left side. The anomalous inner core rotation ($\Delta\Omega_{IC} = 2.55°/\text{yr}$) is indicated by the darker shading of the angular velocity contours inside the inner core relative to the surrounding fluid ($\Delta\Omega_{TW} = 3°/\text{yr}$). The maximum toroidal field is 17 mT.

tion of the thermal wind velocity. In Figure 8 the maximum toroidal field $B_{T\text{max}}$ is plotted versus $\Delta\Omega_{IC}$, the seismically observable inner core rotation rate produced by the thermal wind models. These relations are linear because both variables linearly vary with $\Delta\Omega_{TW}$ in model 1 or with $\Delta\Omega_{XW}$ in model 2. We find the following relationships between the maximum induced toroidal field intensity and the anomalous rotation rate of the inner core:

$$B_{T\text{max}} = \begin{cases} 28.4\,\Delta\Omega_{IC} & \text{Model 1a} \\ 6.7\,\Delta\Omega_{IC} & \text{Model 1b} \\ 41.8\,\Delta\Omega_{IC} & \text{Model 2a} \\ 16.4\,\Delta\Omega_{IC} & \text{Model 2b} \\ 17.9\,\Delta\Omega_{IC} & \text{Analytical model} \end{cases} \quad (25)$$

The maximum induced toroidal field depends strongly on the flow field and the structure of the poloidal field inside the core.

Table 3. Results of Numerical Simulations of Anomalous Inner Core Rotation and Toroidal Field Generation

Model	$\Delta\Omega_{\text{max}}$, °/yr	$\Delta\Omega_{IC}$, °/yr	$B_{T\text{max}}$, mT	P_J, GW
1a	3.0	2.13	60.8	571.1
1a	1.0	0.71	20.3	63.5
1b	3.0	2.56	17.3	53.2
1b	1.0	0.85	5.8	6.0
2a	3.0	1.87	78.3	899.4
2a	1.0	0.62	26.1	101.6
2b	3.0	2.12	34.6	194.3
2b	1.0	0.71	11.5	26.6
3	−0.13	−0.013	3.2	4.7

$\Delta\Omega_{\text{max}}$ is the maximum imposed angular flow velocity in a simulation, $\Delta\Omega_{IC}$ is the resultant steady state anomalous inner core rotation rate, $B_{T\text{max}}$ is the maximum induced toroidal field value at steady state, and P_J is the steady state Joule dissipation.

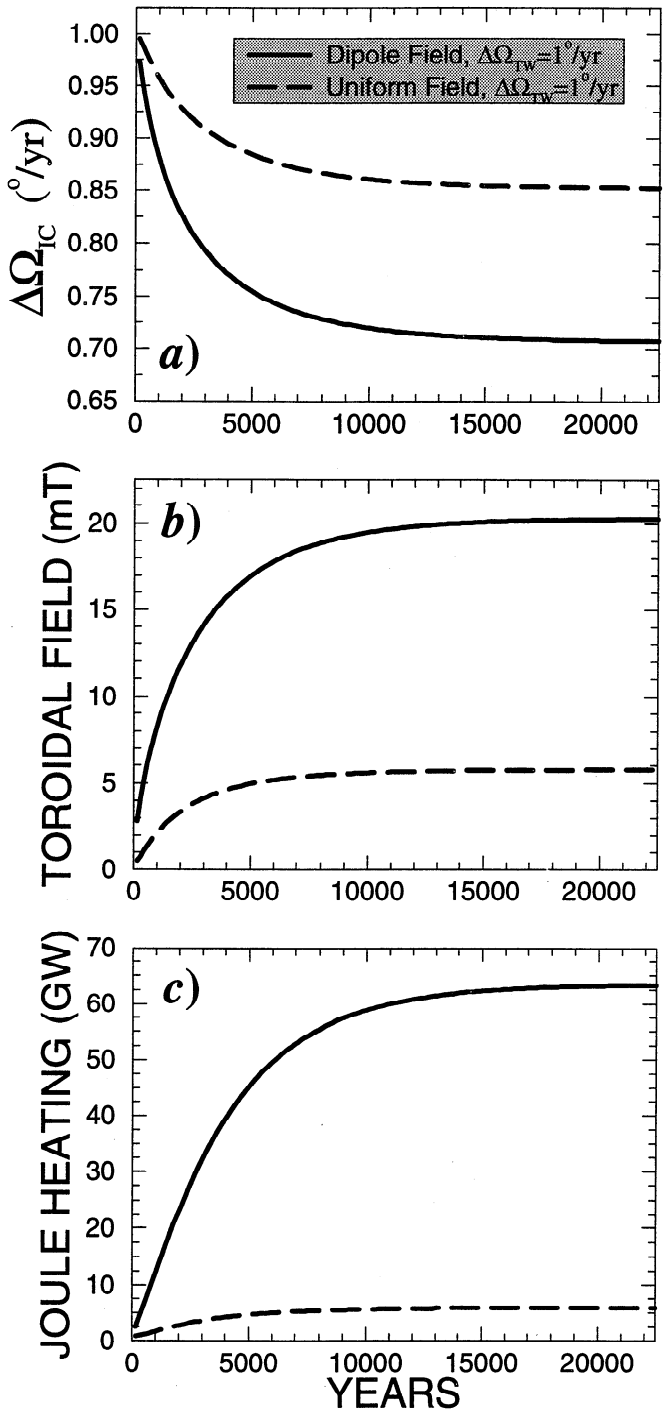

Figure 5. Time series plots of (a) the anomalous rotation of the inner core $\Delta\Omega_{IC}$, (b) the maximum induced toroidal magnetic field $B_{T\max}$, and (c) the Joule heating in the core resulting from a 1°/yr thermal wind acting on a current-carrying dipole and a uniform poloidal magnetic field. The calculations were made using a 120 × 120 grid for 25,000 simulated years. Steady state is reached after approximately 20,000 years.

6.3. Results for Westward Drift Flow

Figure 9 shows the results of the westward drift calculations (model 3) after 25,000 years of simulated time. As in Figures 2, 4, 6, and 7, the right side shows shaded contours of angular velocity as a function of position in the core and line contours of the imposed poloidal magnetic field. The left side shows the induced toroidal magnetic field.

Qualitative and quantitative differences are apparent in comparing Figure 9 with the thermal wind calculations shown in Figures 2, 4, 6, and 7. The inner core is almost at rest with respect to the mantle, having a westward (retrograde) rotation rate of −0.013°/yr as shown in Figure 10b. The toroidal field is concentrated outside of the tangent cylinder and attains a maximum value of roughly 5 mT (Figure 10c), typical of toroidal field amplitudes in the dynamo model of *Kuang and Bloxham* [1997]. Figure 10d shows the Joule heat production in the core equilibrating to a value just under 5 GW in this simulation.

Jackson [1998] inferred the flow velocities inside the tangent cylinder to be between $\omega = -0.09°$/yr and $+0.22°$/yr. Adding a tangent cylinder flow of this magnitude will not affect the results of the westward drift model.

Figure 11 shows two magnetic field lines inside the Earth's core at steady state. The thin, inner field line is produced by a thermal wind simulation (model 1a with $\Delta\Omega_{TW}$=3°/yr), whereas the thick, outer field line is generated in a simulation of the westward drift flow (model 3). In both simulations the current-carrying dipole field model has been imposed. The westward drift field line enters the core at ($r = R_C$, $\theta = \pi/3$, $\phi \simeq \pi/2$) and exits the core at ($r = R_C$, $\theta = 2\pi/3$, $\phi \simeq \pi/2$). The thermal wind field line enters the core at ($r = R_C$, $\theta = \pi/6$, $\phi = 0$) and exits at ($r = R_C$, $\theta = 5\pi/6$, $\phi = 0$). The two field lines are located in different parts of the core such that each line passes close to the region of maximum toroidal field induction in that particular flow simulation.

Initially, the field lines were purely poloidal, but at the time shown, after 28,000 simulated years, the equilibrated magnetic fields have been wound up by the shearing fluid motions in the outer core, resulting in both poloidal and toroidal magnetic field components. The thin, inner field line produced in a thermal wind simulation has been wound into a dominantly toroidal magnetic field that lies mostly within the tangent cylinder. This field line penetrates the inner core near the equator. The thick, outer field line produced by the westward drift model is situated well outside the tangent cylinder. Though still dominantly toroidal, the magnetic field produced by the westward drift is much weaker than that of the thermal wind.

7. Spin-Up of the Inner Core

Gubbins [1981] calculated the period of rotational oscillation of the inner core subject to electromagnetic torques and found that in the presence of a uniform 0.5 mT poloidal field, oscillations of the inner core have a period of approximately 6 years and a decay time of

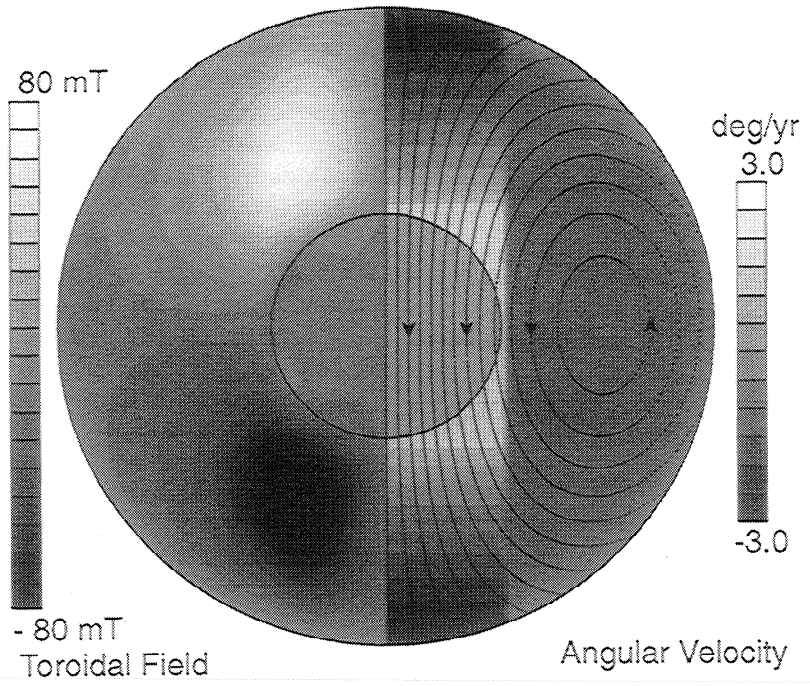

Figure 6. Steady state results of the model with a current-carrying dipolar magnetic field and the 3°/yr X wind flow (model 2a). Contours of angular velocity relative to the mantle of the outer core fluid flow and the solid inner core are shown on the right side. Dipole field lines are superimposed on the angular velocity contours. Shaded contours of the induced toroidal field in milliteslas are shown on the left side. The anomalous inner core rotation ($\Delta\Omega_{IC} = 1.87°/\mathrm{yr}$) is indicated by the darker shading of the angular velocity contours inside the inner core relative to the surrounding fluid ($\Delta\Omega_{XW} = 3°/\mathrm{yr}$). The maximum toroidal field value is 78 mT.

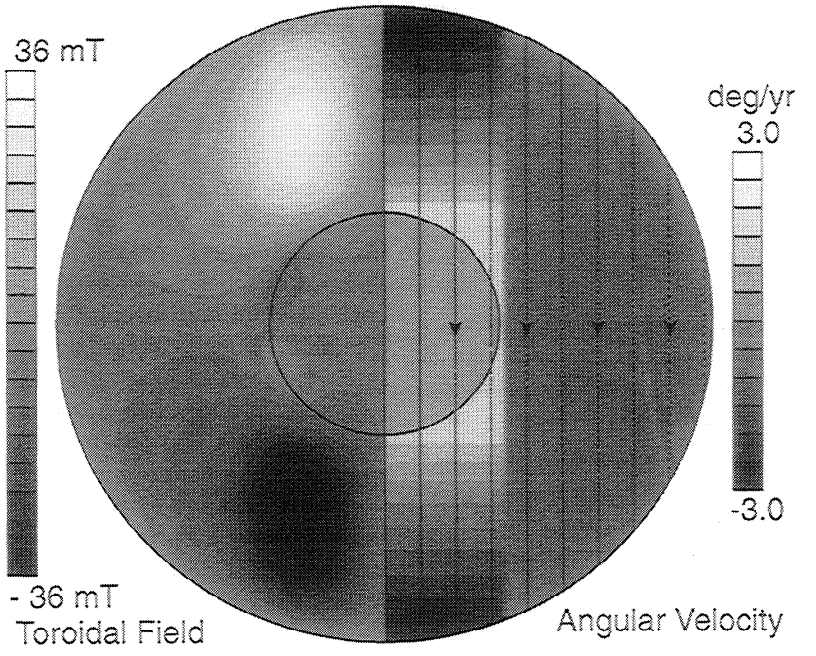

Figure 7. Steady state results of the model with a uniform $\hat{z}$ poloidal magnetic field and the 3°/yr X wind flow (model 2b). Contours of angular velocity relative to the mantle of the outer core fluid flow and the solid inner core are shown on the right side. Uniform $\hat{z}$ field lines are superimposed on the angular velocity contours. Shaded contours of the induced toroidal field in milliteslas are shown on the left side. The anomalous inner core rotation ($\Delta\Omega_{IC} = 2.13°/\mathrm{yr}$) is indicated by the darker shading of the angular velocity contours inside the inner core relative to the surrounding fluid ($\Delta\Omega_{TW} = 3°/\mathrm{yr}$). The maximum toroidal field is 35 mT.

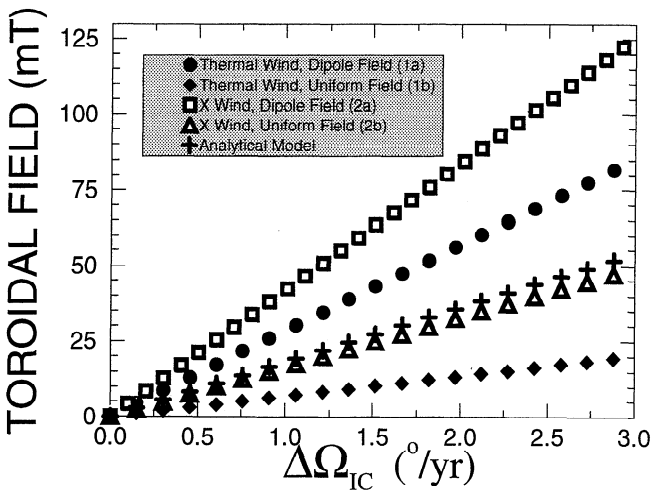

Figure 8. Maximum toroidal magnetic field $B_{T\max}$ versus steady state anomalous inner core rotation rate $\Delta\Omega_{IC}$ for five different models. $B_{T\max}$ varies linearly as a function of the strength of $\Delta\Omega_{IC}$ in the numerical models 1a, 1b, 2a, and 2b as well as in the analytical model of *Aurnou et al.* [1996].

approximately 11 years. Gubbins also found the length scale of the ICB magnetic boundary layers to be 15 km. Gubbins neglected the viscous torque on the inner core because he estimated it be 3-4 orders of magnitude less than the inner core electromagnetic torque, which agrees with the recent numerical calculations of *Dormy et al.* [1998].

We have carried out numerical calculations to determine the spin-up behavior of the inner core under the action of electromagnetic torques in our model. These calculations were begun by fixing the strength of the poloidal field B_o in (12) and (14) and the thermal wind at $\Delta\Omega_{TW}$. The inner core rotation rate $\Delta\Omega_{IC}$ and the toroidal magnetic field were both initially zero as in all the other calculations.

The results of the spin-up calculations are shown in Figure 12. All the calculations were carried out using a 3°/yr thermal wind except in Figure 12b. Figure 12a compares the spin-up processes occurring for the different poloidal field models with $B_o = -0.37$ mT in (12) and (14). The spin-up time for the uniform magnetic field model is roughly 25 years, while the spin-up of the current-carrying dipole model is roughly half that value at close to 12 years. Here we define the spin-up time as the time taken for the inner core to reach a quasi-steady rotation rate.

Figure 12b contrasts the spin-up of the inner core subjected to two different thermal wind strengths of 1.1°/yr and 3°/yr. The spin-up oscillations are in phase and, thus, $\Delta\Omega_{TW}$ only controls the final angular velocity of the inner core.

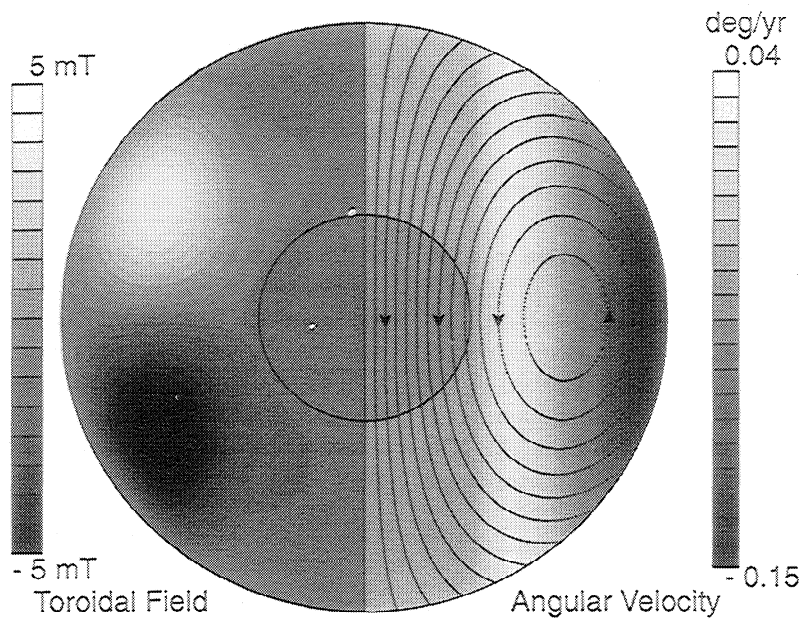

Figure 9. Steady state results of the model with a current-carrying dipolar magnetic field and the concentric, cylindrical fluid flow model derived from geomagnetic westward drift (model 3). Contours of angular velocity relative to the mantle of the outer core fluid flow and the solid inner core are shown on the right side. Current-carrying dipole field lines are superimposed on the angular velocity contours. Shaded contours of the induced toroidal field in milliteslas are shown on the left side. The inner core rotation is retrograde in this model, $\Delta\Omega_{IC} = -0.013$°/yr, as is indicated by the darker shading of the angular velocity contours inside the inner core relative to the neighboring fluid. The fluid inside the tangent cylinder is motionless in this flow model. The maximum toroidal field is 5 mT.

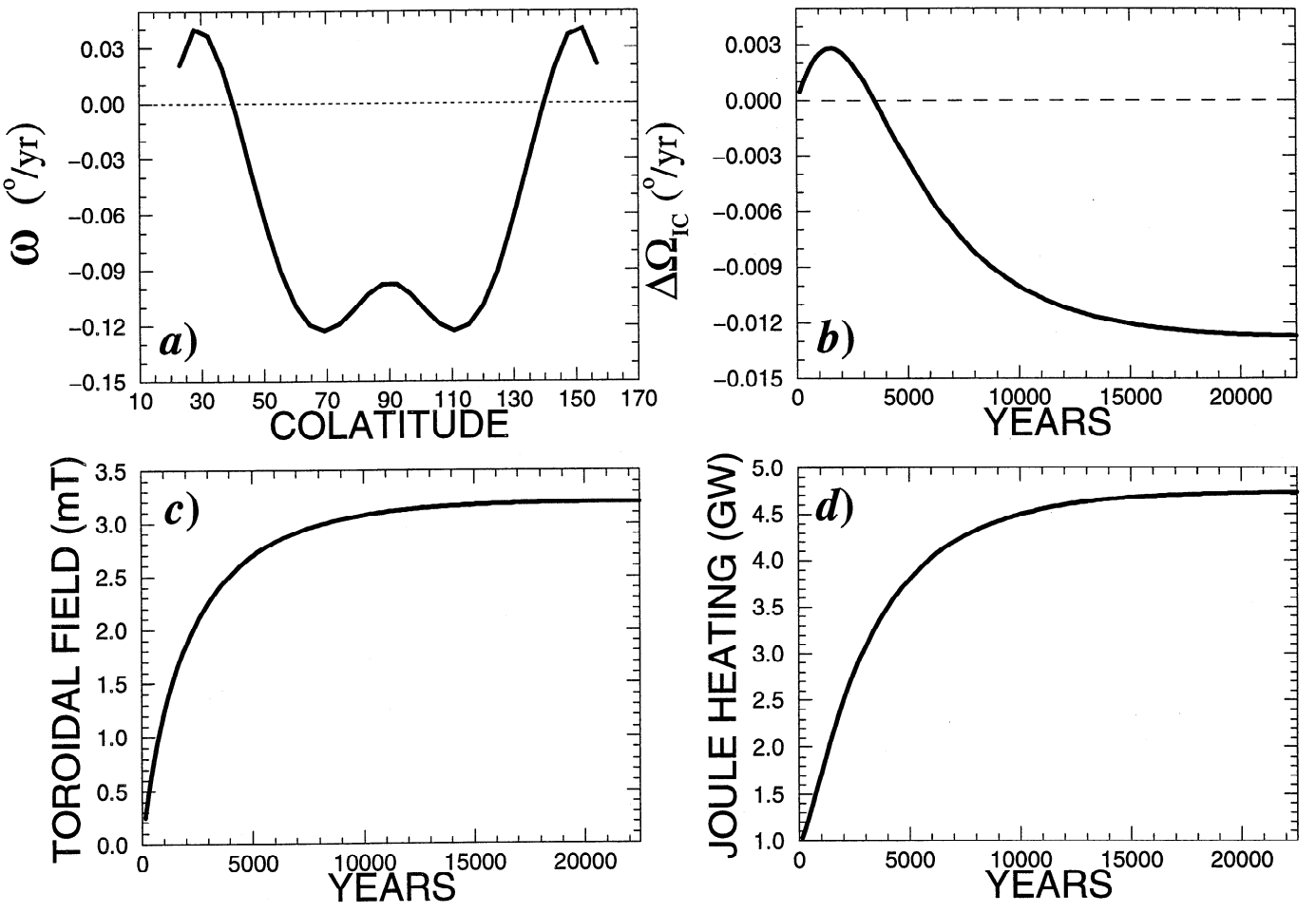

Figure 10. (a) Angular velocity $\omega(s)$ used in flow model 3, derived from geomagnetic westward drift (adapted from *Jault et al.* [1988]), (b) time series of the anomalous rotation of the inner core $\Delta\Omega_{IC}$, (c) the maximum induced toroidal field $B_{T\max}$, and (d) the Joule heating produced by the interaction of this flow field with the current-carrying dipole field model.

Figure 12c demonstrates how the spin-up process varies as a function of the strength of the uniform $\hat{z}$ poloidal magnetic field. Stronger poloidal fields generate stronger magnetic torques which increase the oscillation frequency of the inner core. This increase in the inner core oscillation frequency leads to thinner magnetic boundary layers that efficiently diffuse the ICB magnetic field so that the inner core equilibrates faster to the angular velocity of the surrounding fluid.

The highest value for the strength of the uniform $\hat{z}$ magnetic field used in Figure 12c is $B_o = -1.07$ mT, which generates maximal inner core torques of the order of 10^{18} Nm. When $B_o = -0.37$ mT in (12), the strength of the poloidal magnetic field on the ICB is also -1.07 mT, as shown in Figure 13. Comparing the spin-up for the current-carrying dipole field model having $B_o = -0.37$ mT in Figure 12a with the spin-up for the uniform $\hat{z}$ field model having $B_o = -1.07$ mT in Figure 12c, we see that their spin-up time series are identical. Thus the strength of the poloidal magnetic field on the ICB is the dominant controlling mechanism of the inner core spin-up process.

Because the control of the spin-up process occurs in the magnetic boundary layer surrounding the ICB, the numerical domain was restricted in these calculations to a much smaller spherical shell centered around the ICB. An estimate for the thickness of an appropriate computational shell is the thickness of the magnetic boundary layer

$$\delta = \sqrt{\frac{\eta}{\omega}} \simeq 20 \text{ km} \tag{26}$$

based on $\eta = 2.65$ m^2/s from Table 1 and the angular frequency of the oscillations, $\omega = 2\pi/T$, with oscillation period $T \simeq 20$ years. This agrees with the length scale used by *Gubbins* [1981]. After some experimentation we have adopted a shell of thickness $0.1R_C \simeq 350$ km, which extends roughly 10 boundary layer thicknesses on either side of the ICB. The shell calculations were run using the uniform poloidal field. The shell grid used is 50×50. The current-carrying dipolar field was tested using the full computational grid at much higher radial

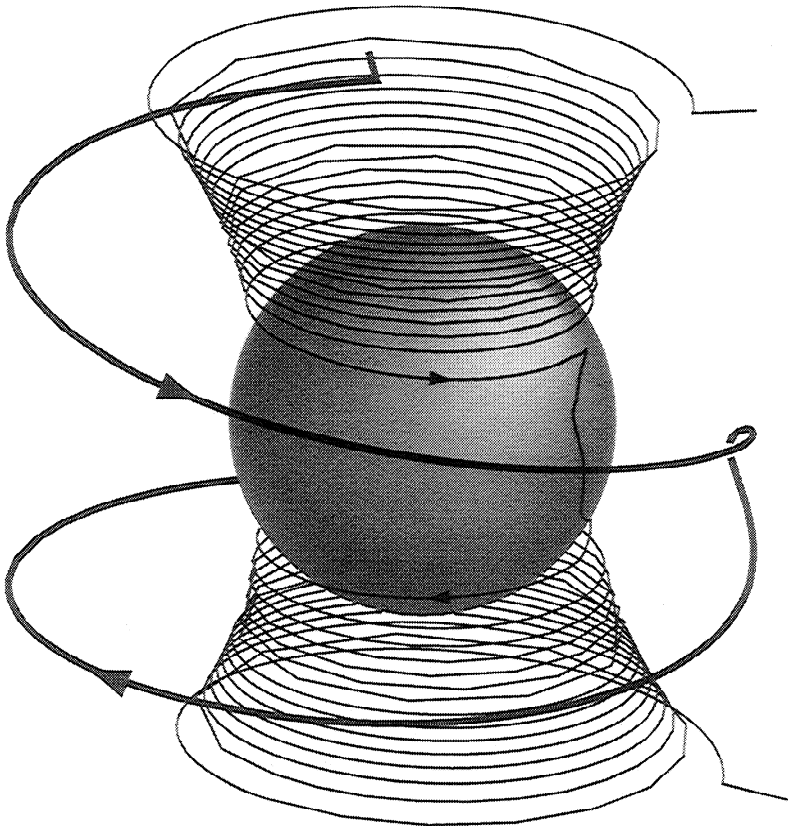

Figure 11. Geometry of magnetic field lines traversing the core. The thin, inner line is obtained at steady state from the thermal wind flow (model 1a) with $\Delta\Omega_{TW} = 3°/\text{yr}$. The thick, outer field line is obtained at steady state from the westward drift flow (model 3).

resolution, 395 × 120, than for the toroidal field equilibration calculations discussed in sections 6.1 through 6.3.

Figure 12d shows the results of the shell calculations. By doubling the θ resolution to 50 × 100, no change occurs in the spin-up, indicating that the boundary layer is well resolved in θ. Doubling the radial resolution to 100 × 50 produces a slightly more damped solution, indicating that the thickness of the magnetic boundary layer is even less than 20 km, and our fine grid is barely adequate to resolve the boundary layer properly. This seems to agree with the work of *Glatzmaier and Roberts* [1996] where their calculations produce a heavily damped spin-up which equilibrates within roughly 2 years.

8. Discussion

8.1. Physical Mechanism

The combination of poloidal and toroidal magnetic fields at the ICB results in torques on the inner core (equation (3)). Differential flows in the outer core induce toroidal fields that diffuse onto the ICB and produce torques on the inner core. The difference in angular velocity across the ICB strongly shears any magnetic field lines that intersect the ICB surface. The toroidal field generated at this ICB shear layer leads to a second set of electromagnetic restoring torques. These secondary torques couple the inner core to the surrounding fluid so that the angular velocity of the inner core equilibrates to a value close to the angular velocity, or some weighted average of the angular velocity, of the fluid surrounding the inner core. Thus the two torques balance in steady state, with the inner core lagging slightly behind the motion of the surrounding fluid.

8.2. Model Comparisons

8.2.1. Analytical model. The steady state analytical model of inner core superrotation of *Aurnou et al.* [1996] produced a prograde superrotation of the inner core by imposing a prograde thermal wind inside the tangent cylinder. Their thermal wind flow field is similar to the one used here (model 1) except that the analytical model did not have a Stewartson layer at the tangent cylinder boundary. In the analytical model the angular velocity of the inner core was prograde and lagged the surrounding fluid by approximately 14%. Steady state toroidal fields of 20-55 mT were produced by inner core rotation rates $\Delta\Omega_{IC}$ of 1.1° to 3°/yr, respectively. It was also shown that a temperature difference across the tangent cylinder of $\sim 5 \times 10^{-4}$ K is required to set up an inner core superrotation rate of 1.1°/yr.

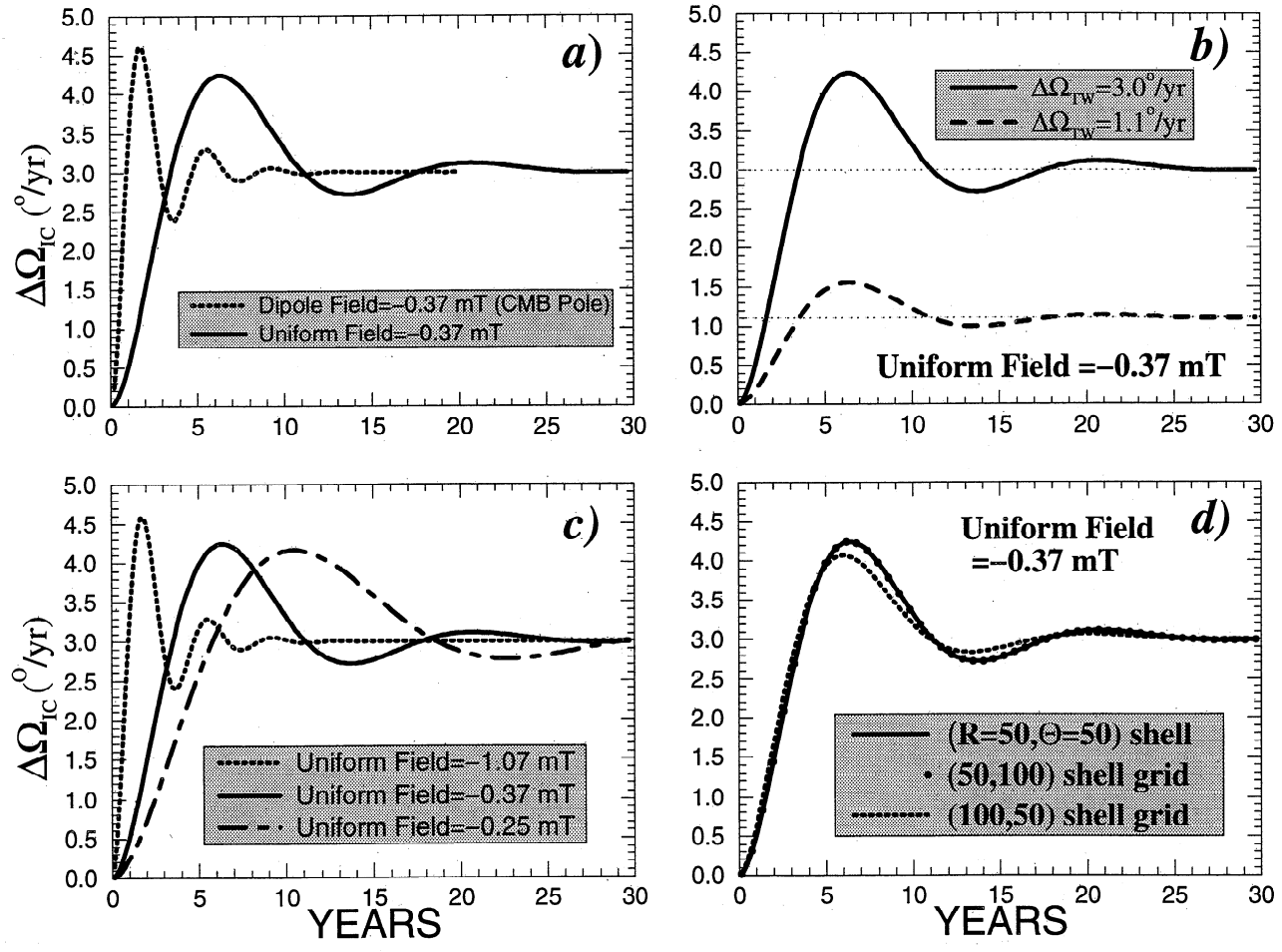

Figure 12. Evolution of the anomalous inner core angular velocity $\Delta\Omega_{IC}$ versus time for (a) various poloidal magnctic field geometries and (Figures 12a and 12c) strengths, (b) differences in the strength of the imposed thermal wind $\Delta\Omega_{TW}$, and (d) the size and density of the computational grid.

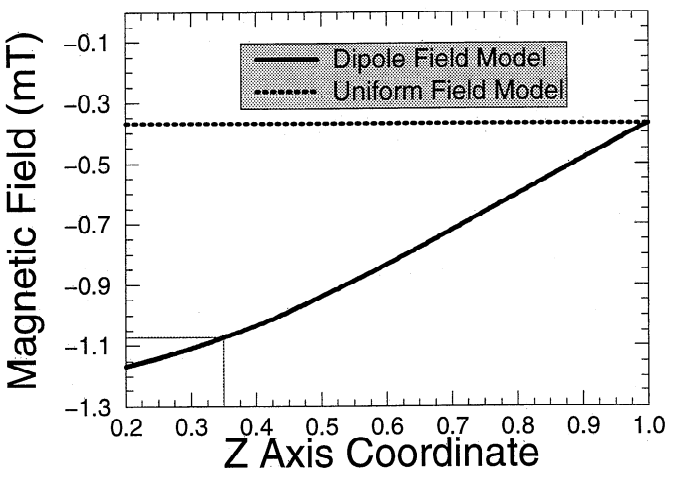

Figure 13. Magnetic field strength versus the z axis coordinate inside the Earth's core. The magnetic field strength increases with depth for the current-carrying dipole model and is constant for the uniform $\hat{z}$ field model.

8.2.2. Toroidal magnetic fields. The westward drift flow (model 3) produces an equilibrium toroidal field with a different spatial structure from the thermal wind flows (models 1 and 2). All the flow models produce large-scale, large-amplitude toroidal fields, but the seat of the toroidal field produced by the thermal wind models is inside the tangent cylinder, while the westward drift model produces a toroidal field centered well outside the tangent cylinder (compare Figures 2, 4, 6, 7, 9, and 11). In the westward drift flow model the sign of the induced toroidal field is the same as that produced by a "hot" tangent cylinder thermal wind with the toroidal magnetic field directed to the east in the northern hemisphere and directed to the west in the southern hemisphere, as illustrated in Figure 9. The electromagnetic torque produced by this magnetic field configuration drives the inner core into retrograde motion. Because the fluid within the tangent cylinder is completely motionless in this model, the inner core comes into torque equilibrium with a very

small westward angular velocity of -0.013°/yr (Figure 10b). This difference between the values of the inner core rotation rate predicted by the thermal wind models, $\Delta\Omega_{IC} \simeq +2°/\mathrm{yr}$, and the westward drift model, $\Delta\Omega_{IC} \simeq -0.01°/\mathrm{yr}$, may allow for observational tests of the two flow models.

While the comparisons between the westward drift model and the thermal wind models are fairly straightforward, as seen in Figure 11, the differences between the thermal wind models 1a and 1b are more subtle, and understanding these differences can shed light on the processes occurring in the electromagnetic torque problem. The induced toroidal field in model 1a differs from model 1b because the Stewartson layer acts as a source of toroidal field only in model 1a. The horizontal fluid shears in the Stewartson layer couple with the horizontal components of the magnetic field in model 1a to produce strong toroidal fields inside the Stewartson layer. In model 1b the uniform $\hat{z}$ magnetic field vector is completely insensitive to these horizontal shears. Thus the Stewartson layer increases the strength of the toroidal field in model 1a and acts to push the location of the maximum toroidal field values out in s toward the tangent cylinder wall. The toroidal field production in the Stewartson layer also allows one to trace the outline of the tangent cylinder in the toroidal field contours of model 1a (see Figure 2). No detectable signs of the tangent cylinder are visible in the toroidal field generated by model 1b (see Figure 4).

The difference in the induced toroidal fields between models 1a and 1b also occurs because the strength of the poloidal field is spatially variable in model 1a while remaining fixed in model 1b. Figure 13 compares the strength of the poloidal field between model 1a and model 1b as a function of height z in the core. The strength of the current-carrying dipole field triples in value from the CMB to the ICB, which leads to stronger induced toroidal fields occurring deeper within the core in model 1a as compared to model 1b.

The gradient in $\hat{z}$ of the imposed thermal wind is twice as strong in model 2 as in model 1. Thus the results in Table 3 show that model 2 produces greater lag of the inner core behind the surrounding fluid, stronger induced toroidal fields, and higher Joule heating in comparison to model 1. A second difference between the thermal wind models is that in model 2a the intersection of the retrograde region of the X wind flow with the Stewartson layer will create toroidal field of the opposite sense as found in the rest of that hemisphere. Thus the symmetric X shape of the thermal wind in model 2a leads to a toroidal field that is less concentrated near the edge of the tangent cylinder (see Figures 2 and 6).

In the uniform $\hat{z}$ magnetic field models the $\hat{z}$ shear of the tangent cylinder fluid is twice as strong in model 2b as the shear imposed in model 1b. Since this shear is the only source of toroidal field generation in the fluid outer core for these two models, the lag of the inner core as well as $B_{T_{\mathrm{max}}}$ in model 2b are twice that of model 1b.

The toroidal field generated in the uniform $\hat{z}$ field model 1b is about one third the toroidal field found in the analytical solution. This is due to the treatment of diffusion in the different models. In the analytical model diffusion occurs solely from the cylindrical volume of the tangent cylinder. The diffusion is only a function of radius s with a zero field boundary condition on the rotation axis and a zero radial flux condition on the tangent cylinder boundary. This is much more restrictive than the numerical problem where diffusion is allowed to occur throughout the sphere with a zero toroidal field condition on the rotation axis and at the CMB.

The steady state toroidal field does not go to zero on the ICB in any of the numerical models even though the net electromagnetic torque on the inner core does vanish at equilibrium. The steady state ICB toroidal fields, which are of the order of $10^{-2}B_{T_{\mathrm{max}}}$, are antisymmetric across the equator. If a purely positive ICB toroidal field existed in the northern hemisphere and a purely negative ICB toroidal field existed in the southern hemisphere then a retrograde electromagnetic torque would necessarily result (see equation (3)). However, there is also a change in the sign of the ICB toroidal field within each hemisphere in Figures 2, 4, 6, and 7 such that Γ_N, the northern hemisphere net axial torque

$$\Gamma_N = \int_0^{2\pi} \int_0^{\pi/2} \frac{R_I^3}{\mu} B_r B_\phi \sin^2\theta \, d\theta d\phi \qquad (27)$$

and Γ_S, the southern hemisphere net axial torque

$$\Gamma_S = \int_0^{2\pi} \int_{\pi/2}^{\pi} \frac{R_I^3}{\mu} B_r B_\phi \sin^2\theta \, d\theta d\phi \qquad (28)$$

are separately equal to zero: $\Gamma_N = \Gamma_S = 0$. This result is also found in the dynamo simulations of *Glatzmaier and Roberts* [1995a, b, 1996].

8.2.3. Inner core rotation. The anomalous rotation rate of the inner core, $\Delta\Omega_{IC}$, is seen to decrease whenever the effects of the Stewartson layer or depth-dependent poloidal field strength act to induce larger toroidal fields $B_{T_{\mathrm{max}}}$ in the bulk of the core. The increase in toroidal field strength requires $\Delta\Omega_{IC}$ to decrease so that the lag between the inner core and the surrounding fluid increases. This increase in lag generates a stronger opposing toroidal field on the ICB needed to establish a torque balance.

The westward drift flow model produces a steady state inner core rotation rate that is retrograde. Before reaching this steady state, Figure 10b shows that the inner core rotates eastward in the prograde direction. This initial prograde rotation of the inner core occurs because the magnetic field that first diffuses onto the ICB is induced by the reversed shear in the flow modeled at high latitudes in Figure 10a. After about 3500

years the magnetic field induced by the main shear in the westward drift model, located between 30° and 150° colatitude in 10a, diffuses onto the ICB and reverses the direction of the inner core rotation anomaly from prograde to retrograde.

The prograde rotation rate of the inner core, $\Delta\Omega_{IC}$, is $0.85\Delta\Omega_{TW}$ in the case of a uniform field and $0.86\Delta\Omega_{TW}$ in the analytical model. The close match between the anomalous rotation rate for the analytical model and the uniform field model 1b is coincidental. The approximations made in the analytical model happen to produce almost the same inner core rotation as found for the uniform field model while generating a very different toroidal field in amplitude and spatial structure.

It should be reiterated that our simulations use kinematic models of the fluid flow in the outer core. In a fully dynamical simulation the electromagnetic torques act to change the flow field itself. For example, the electromagnetic torques that affect only the inner core rotation in model 3 would likely also spin-up the fluid within the tangent cylinder in a dynamical simulation.

8.3. Joule Heat Production

The Joule heat production as a function of time is plotted in Figures 3c, 5c, and 10d. Steady state Joule heating rates are given for all the models in Table 3. The Joule heating P_J varies as the square of the maximum induced toroidal field value, according to the following formulas:

$$P_J = \begin{cases} 0.149(B_{T\max})^2 & \text{Model 1a} \\ 0.148(B_{T\max})^2 & \text{Model 1b} \\ 0.142(B_{T\max})^2 & \text{Model 2a} \\ 0.148(B_{T\max})^2 & \text{Model 2b} \\ 0.340(B_{T\max})^2 & \text{Model 3} \end{cases} \quad (29)$$

where $P_J = \int_{\text{core}} \frac{\eta}{\mu}(\nabla \times \mathbf{B})^2 dV$ is the total Joule heat production in the models shown in Figures and 3c, 5c, and 10d. $B_{T\max}$ is the maximum induced toroidal field in Figures 3b, 5b, and 10c. The proportionality coefficients in (29) are the slopes of linear regressions of the time series of the joule dissipation P_J versus the square of the maximum induced toroidal field $(B_{T\max})^2$ for each of the models shown. All the linear regressions gave correlations coefficients $0.999 < R^2 < 1$. The proportionality coefficient in (29) for the westward drift model is more than twice that of the thermal wind models. This is due to the difference in the spatial structure of the induced fields produced by the two flow models: the normalized moment of the magnetic energy is greater in the case of the westward drift flow because the field is produced outside the tangent cylinder at greater s values. The fact that the coefficients for the four thermal wind models differ by less than 5% demonstrates the close correlation between their gross field structures.

The Joule heat production in the core is related to the total heat flux at the CMB as

$$P_J = \varepsilon P_{\text{CMB}} \quad (30)$$

where P_{CMB} is the total outward heat flux evaluated at the CMB and ε is an efficiency factor [*Backus*, 1975; *Hewitt et al.*, 1975; *Lister and Buffett*, 1995]. *Lister and Buffett* [1995] have estimated $P_{\text{CMB}} = 3$ TW and $\varepsilon = 0.2$, so that a typical estimate of the Joule dissipation in the core is roughly 600 GW.

The interaction of the current-carrying dipole field model with the 3°/yr thermal wind flow model produces nearly 600 GW and the 3°/yr X wind flow model produces 900 GW of Ohmic dissipation, close to and over the thermodynamic limit estimated by *Lister and Buffet* [1995]. Considering that we do not take into account Joule heat production at small length scales as is likely to occur in the core [*Brito et al.*, 1996], energy considerations suggest an upper bound close to 3°/yr for the strength of thermal wind flows inside the tangent cylinder.

8.4. Stewartson Layer

The results of models with differing thickness of the Stewartson layer are given in Table 4. The flow model used in these simulations is the thermal wind model 1a with a maximum angular velocity of $\Delta\Omega_{TW} = 3°/\text{yr}$.

Table 4. Results of Numerical Simulations of Model 1a with $\Delta\Omega_{TW} = 3°/\text{yr}$ Subject to Variations in Thickness of the Stewartson Layer

Layer Thickness, km	$\Delta\Omega_{IC}$, °/yr	$B_{T\max}$, mT	P_J, GW	$P_J/(B_{T\max})^2$, GW/mT^2
50	2.150	58.82	519	0.145
100	2.129	60.46	565	0.149
150	2.108	62.17	613	0.154
200	2.087	64.05	663	0.157
250	2.068	66.01	714	0.159

Layer thickness is the thickness of the Stewartson layer truncation in kilometers. $\Delta\Omega_{IC}$ is the steady state anomalous rotation rate of the inner core, $B_{T\max}$ is the maximum induced toroidal field at steady state, and P_J is the Joule dissipation in the core. The last column of data is the slope determined from a linear regression analysis of the time series of P_J as a function of $(B_{T\max})^2$.

The anomalous inner core rotation rate, $\Delta\Omega_{IC}$ in Table 4, decreases linearly with increasing Stewartson layer thickness while $B_{T\max}$ linearly increases with the thickness of the layer. Thus, in flow model 1a, the Stewartson layer acts as a source of toroidal magnetic field which increases in source strength with layer thickness.

In the last column of Table 4 we show slope from the linear regression of the time series of the joule dissipation P_J versus the square of the maximum induced toroidal field $(B_{T\max})^2$ for each of the Stewartson layer models. As in section 8.3, all the linear regressions gave correlations coefficients $0.999 < R^2 < 1$. The ratio $P_J/(B_{T\max})^2$ increases with the Stewartson layer thickness because the moment of the magnetic energy increases in the core with increasing Stewartson layer thickness.

9. Conclusions

The combination of toroidal and poloidal magnetic fields exerts electromagnetic torques on the solid inner core, resulting in its anomalous spin. Our calculations indicate a close relationship between the anomalous rotation of the inner core and the generation of toroidal magnetic field by the ω effect. The toroidal magnetic field is induced from the poloidal magnetic field by the azimuthal motions of the outer core fluid. In equilibrium, two opposing electromagnetic torques couple the inner core to the fluid motion such that the anomalous angular velocity of the inner core is proportional to the average angular velocity of the adjacent fluid.

Azimuthal motion consisting of cylindrical flow on geostrophic contours inferred from the geomagnetic westward drift induces toroidal magnetic field concentrated outside the tangent cylinder of the inner core and results in a small retrograde inner core rotation anomaly. This behavior is not compatible with the seismic interpretations of a prograde inner core rotation anomaly. In contrast, thermal wind azimuthal flow resulting from a positive temperature anomaly within the inner core tangent cylinder can easily account for the seismically inferred inner core rotation anomaly. This mechanism connects the toroidal field, which is concentrated along a Stewartson shear layer located at the inner core tangent cylinder, to the anomalous inner core rotation rate. For the current-carrying dipole field and the X wind flow model with $\Delta\Omega_{IC} = 3°/yr$ (*Su et al.*, [1996]), $B_{T\max} \simeq 125$ mT; for $\Delta\Omega_{IC} = 1.1°/yr$ (*Song and Richards*, [1996]), $B_{T\max} \simeq 47$ mT; for $\Delta\Omega_{IC} = 0.25°/yr$ (*Creager*, [1997]), $B_{T\max} \simeq 10$ mT. Time-dependent calculations demonstrate that if the electromagnetic torque equilibrium is disturbed, the inner core rotation adjusts via damped oscillations having a periodicity of about 4 years and a spin-up time close to 12 years, in accord with both the analytical model of *Gubbins* [1981] and the *Glatzmaier and Roberts* [1996] numerical dynamo model.

Acknowledgments. This research was supported by the NSF Geophysics Program and the IGPP at Los Alamos. The authors wish to thank Andrew Jackson and two anonymous referees for useful comments and Jim Buttles for his help with the 3-D graphics.

References

Abramowitz, M., and I.A. Stegun, *Handbook of Mathematical Functions*, 1046 pp., Dover, Mineola, NY, 1964.

Aurnou, J.M., D. Brito, and P.L. Olson, Mechanics of inner core super-rotation, *Geophys. Res. Lett.*, *23*, 3401-3404, 1996.

Backus, G.E., Gross thermodynamics of heat engines in the deep interior of Earth, *Proc. Natl. Acad. Sci. U. S. A.*, *72*, 1555-1558, 1975.

Bloxham, J., D. Gubbins, and A. Jackson, Geomagnetic secular variation, *Philos. Trans. R. Soc. London, Ser. A*, *329*, 415-502, 1989.

Brito, D., P. Cardin, H.-C. Nataf, and P.L. Olson, Experiments on Joule heating and the dissipation of energy in the Earth's core, *Geophys. J. Int.*, *127*, 339-347, 1996.

Buffett, B.A., A mechanism for decade fluctuations in the length of day, *Geophys. Res. Lett.*, *23*, 3803-3806, 1996.

Creager, K.C., Inner core rotation rate from small-scale heterogeneity and time-varying travel times, *Science, 278*, 1284-1288, 1997.

Dormy, E., P. Cardin and D. Jault, MHD flow in a slightly differentially rotating spherical shell, with conducting inner core in a dipolar magnetic field, *Earth Planet. Sci. Lett.*, in press, 1998.

Elsasser, W.M., Induction effects in terrestrial magnetism, *Phys. Rev.*, *69*, 106-116, 1946.

Glatzmaier, G.A., and P.H. Roberts, A three-dimensional, self-consistent computer simulation of a geomagnetic reversal, *Nature*, *377*, 203-208, 1995a.

Glatzmaier, G.A., and P.H. Roberts, A three-dimensional convective dynamo solution with rotating and finitely conducting inner core and mantle, *Phys. Earth Planet. Inter.*, *91*, 63-75, 1995b.

Glatzmaier, G.A., and P.H. Roberts, Rotation and magnetism of Earth's inner core, *Science*, *274*, 1887-1891, 1996.

Greenspan, H.P., *The Theory of Rotating Fluids*, 328 pp., Cambridge Univ. Press, New York, 1968.

Gubbins, D., Rotation of the inner core, *J. Geophys. Res.*, *86*, 11695-11699, 1981.

Hewitt, J.M., D.P. McKenzie, and N.O. Weiss, Dissipative heating in convective flows, *J. Fluid Mech.*, *68*, 721-738, 1975.

Hollerbach, R., On the theory of the geodynamo, *Phys. Earth Planet. Inter.*, *98*, 163-185, 1996.

IAGA Division V, Working Group 8, *Eos Trans. AGU*, *77*, 153, 1996.

Jault, D., C. Gire, and J.L. Le Moüel, Westward drift, core motions and exchanges of angular momentum between the core and mantle, *Nature*, *333*, 353-356, 1988.

Jackson, A., Time dependency of tangentially-geostrophic core surface motions, *Phys. Earth Planet. Inter.*, in press, 1998.

Kleeorin, N., I. Rogachevskii, A. Ruzmaikin, A.M. Soward, and S. Starchenko, Axisymmetric flow between differentially rotating spheres in a dipole magnetic field, *J. Fluid Mech.*, *344*, 213-244, 1997.

Kuang, W., and J. Bloxham, An Earth-like numerical dynamo model, *Nature*, *389*, 371-374, 1997.

Lister, J.R., and B.A. Buffett, The strength and efficiency of thermal and compositional convection in the geodynamo, *Phys. Earth Planet. Inter.*, *91*, 17-30, 1995.

Moffatt, H.K., *Magnetic Field Generation in Electrically Conducting Fluids*, 343 pp., Cambridge Univ. Press, New York, 1978.

Olson, P.L., and G.A. Glatzmaier, Magnetoconvection in a rotating spherical shell: Structure of flow in the outer core, *Phys. Earth Planet. Inter.*, *92*, 109-118, 1995.

Rochester, M.G., Geomagnetic core-mantle coupling, *J. Geophys. Res.*, *67*, 4833-4836, 1962.

Song, X., and P.G. Richards, Observational evidence for differential rotation of the Earth's inner core, *Nature*, *382*, 221-224, 1996.

Su, W.J., A.M. Dziewonski, and R. Jeanloz, Planet within a planet: Rotation of the inner core of the Earth, *Science*, *274*, 1883-1887, 1996.

J. Aurnou and P. Olson, Department of Earth and Planetary Sciences, Johns Hopkins University, Olin Hall, 3400 N. Charles St., Baltimore, MD 21218-2681. (e-mail: aurnou@gibbs.eps.jhu.edu; olson@gibbs.eps.jhu.edu)

D. Brito, LGIT, IRIGM-BP 53, 38041 Grenoble Cedex 09 FRANCE. (e-mail: Daniel.Brito@lgit.obs.ujf-grenoble.fr)

(Received May 7, 1997; revised October 9, 1997; accepted December 10, 1997.)